

Nanosized Fe–Cu–B Alloys and Composites Synthesized in Diphasic Systems

N. Duxin,^{†,‡} N. Brun,[§] P. Bonville,^{||} C. Colliex,^{*,§} and M. P. Pileni^{*,†,‡}

Laboratoire "Structure et Réactivité des Systèmes Interfaciaux", Université Pierre et Marie Curie, URA CNRS 1662, BP 52, 4 place Jussieu, 75005 Paris, France, CEA-DSM-DRECAM Service de Chimie Moléculaire, CEA Saclay, 91191 Gif sur Yvette, Cedex, France, Laboratoire de Physique des Solides, Université Paris-Sud, URA CNRS 002, Bâtiment 510, 91450 Orsay Cedex, France, and CEA-DSM-DRECAM Service de Physique de l'Etat Condensé, CEA Saclay, 91191 Gif sur Yvette, Cedex, France

Received: May 12, 1997; In Final Form: July 8, 1997[®]

A rather homogeneous alloy made of immiscible Fe and Cu was synthesized by using colloidal solutions. The starting materials were a mixture of 30% and 70% of iron(II) (Fe(AOT)₂) and copper(II) (Cu(AOT)₂) bis(2-ethylhexyl)sulfosuccinate, respectively. The nanosized alloys are fairly polydispersed, with sizes ranging from 5 to 15 nm. Varying the ratio of Fe(AOT)₂ to Cu(AOT)₂ induces very marked changes in morphology. The samples were characterized by transmission electron microscopy, X-ray and electron diffraction, ⁵⁷Fe Mössbauer spectroscopy, energy dispersive spectrometry, electron energy loss spectrometry, and room-temperature magnetization measurements.

1. Introduction

Nanostructured materials have attracted great attention because of their unique characteristics for producing ductile materials in intermetallic compounds and for the development of high strain rate superplasticity due to their ultrafine, nanocrystalline grain structure.^{1–3} Such alloys are expected to be useful since they have the advantage that they can be compacted to any shape to serve different purposes as bulk amorphous alloys.⁴ Furthermore, they can be used either for catalytical applications⁵ or for electromagnetic shielding, for magnetic recording, and for advanced engineered material processing.⁶ It is also of interest to study such alloys to determine if the fundamental structure and intrinsic magnetic properties differ from materials of similar compositions.

In the equilibrium states, the solid solubility between Fe and Cu is negligibly small. Their mixing enthalpy is positive, and they form no intermetallic compounds even though their atomic radii are quite similar. However by using vapor-quenching methods such as sputtering, which bypass the liquid phase, the solid solubility can be extended and a Fe–Cu solid solution can be formed over a wide range of composition.^{7,8} This method produces metastable crystalline as well as amorphous alloys. Ball milling is another technique which has been often used to produce metastable Fe–Cu alloys.^{9–14} More recently Fe–Cu alloys were obtained by chemical reduction of divalent metal ions in water.¹⁵

Whatever the preparation mode,^{4,15–20} the crystallographic phase of Fe_xCu_{1–x} depends on the relative iron and copper concentrations used for the synthesis. For 0 ≤ x < 0.6, a face centered cubic (fcc) structure similar to that of copper metal is observed. Under such conditions, alloys are produced. For 0.6 ≤ x ≤ 1, both the face centered cubic (fcc) copper and the body centered cubic (bcc) α-iron phases are observed with formation of alloys and composites. In the chemical reduction of iron ions by sodium borohydride, alloys and composites containing boron are obtained. Reduction of copper ions with sodium

borohydride leads to metallic copper materials without inclusion of boron in the fcc structure.¹⁹ To our knowledge, these alloys have never been characterized on the nanoscale level.

In ball-milled alloys, the alloying driving force is due to the enthalpy stored at the grain boundaries and high-density dislocations. For nanocrystalline alloyed phases, the interfacial energy, occurring with a deformation of the lattice, and dislocations are raising the free energy and can be a driving force for alloying.²⁰ When alloys are formed through chemical reduction, the surface energy can be the driving force. On the other hand, boron insertions are expected to stabilize the metastable Fe–Cu structure.¹⁵

In this work, we used functionalized surfactants such as iron(II) and copper(II) bis(2-ethylhexyl)sulfosuccinate, Fe(AOT)₂ and Cu(AOT)₂, to synthesize alloy derivatives and composites. Transmission electron microscopy, X-ray and electron diffraction, ⁵⁷Fe Mössbauer spectroscopy, energy dispersive spectrometry, electron energy loss spectrometry, and room-temperature magnetization measurements were employed to characterize the products.

2. Experimental Procedure

Products. Sodium bis(2-ethylhexyl)sulfosuccinate, AOT, was from Sigma, isooctane from Fluka (99.5% purity), and NaBH₄ from Alpha Products. All chemicals were used without further purification.

Single-distilled water was passed through a Millipore "MilliQ" system cartridge until its resistivity reached 18 MΩ·cm.

Functionalized Surfactants. Syntheses of divalent bis(2-ethylhexyl)sulfosuccinate, X(AOT)₂, have been described previously.²² In the experiments described here, iron(II) and copper(II) derivatives, Fe(AOT)₂ and Cu(AOT)₂, have been used.

Synthesis of Alloys and Composites. A mixture of Fe(AOT)₂ and Cu(AOT)₂ is solubilized in isooctane to form reverse micelles. The total X(AOT)₂ concentration is kept to 0.1 M. The composition, x, is defined:

$$x = [\text{Fe(AOT)}_2] / \{[\text{Fe(AOT)}_2] + [\text{Cu(AOT)}_2]\}$$

Addition of an equal volume of aqueous phase to the micellar solution induces a phase transition. In the lower part of the

* To whom correspondence should be addressed.

† Université Pierre et Marie Curie.

‡ CEA-DSM-DRECAM Service de Chimie Moléculaire.

§ Université Paris-Sud.

|| CEA-DSM-DRECAM Service de Physique de l'Etat Condensé.

® Abstract published in *Advance ACS Abstracts*, October 1, 1997.

resulting mixture, an anisotropic birefringent phase is observed, and in the upper part, an isotropic non-birefringent reverse micellar phase is formed.

Syntheses are performed in an Ar atmosphere chamber to prevent oxidation. The nanoparticles are obtained by mixing at 300 K with vigorous stirring a 0.1 M $X(\text{AOT})_2$ micellar solution (formed by various amounts, x , of $\text{Fe}(\text{AOT})_2$ and $\text{Cu}(\text{AOT})_2$) with an aqueous solution of 0.4 M sodium borohydride, NaBH_4 . For $x = 0.3$ (alloy formation), 24.6 mL and 57.1 mL of 0.1 M $\text{Fe}(\text{AOT})_2$ and $\text{Cu}(\text{AOT})_2$, respectively, are mixed with 81.6 mL of 0.4 M NaBH_4 . For $x = 0.7$ (composite formation), 35.2 mL of 0.4 M NaBH_4 are added to 24.6 mL and 10.6 mL of 0.1 M $\text{Fe}(\text{AOT})_2$ and $\text{Cu}(\text{AOT})_2$, respectively. Immediately after mixing, a black precipitate appears. It is washed with deaerated isooctane and then with acetone to remove all the surfactant. The precipitate is dried in an Ar atmosphere chamber. Both $\text{Fe}(\text{AOT})_2$ and $\text{Cu}(\text{AOT})_2$ are reduced for x equal to 0.7 and 0.3.

Mössbauer Experiments. The Mössbauer spectra were recorded using a $^{57}\text{Co}^*\text{:Rh}$ γ -ray source ($E_0 = 14.4$ keV) mounted on an electromagnetic drive with a triangular velocity signal. The spectra were least squares fitted to obtain the hyperfine parameters (isomer shift δ , quadrupolar splitting Δ , and hyperfine field H_{hf}). In some cases, a broad hyperfine field distribution is observed. It was fitted by using either a histogram of hyperfine fields with free weights or a Gaussian distribution.

We recall briefly the main characteristics of the ^{57}Fe Mössbauer spectra of iron oxides and iron metallic alloys. The isomer shift values (δ) are given with respect to $\alpha\text{-Fe}$. δ is very sensitive to the Fe oxidation state; for metallic Fe, ionic Fe^{3+} and ionic Fe^{2+} typical values of δ are 0, 0.5, and 1.2 mm/s, respectively. The hyperfine field value at saturation also depends on the oxidation state: for Fe in a metallic environment, $H_{\text{hf}}(T=0) = 250\text{--}350$ kOe (340 kOe for $\alpha\text{-Fe}$) and for Fe^{3+} in an insulating oxide, $H_{\text{hf}}(T=0) = 450\text{--}550$ kOe.

All the spectra reported are zero external field spectra and were recorded in the temperature range 4.2–330 K.

Magnetization Curve. A commercial alternative gradient field magnetometer operating at room temperature in a field up to 1.8 T was used.

X-Ray Diffraction. A Stoe Stadi P goniometer with a Siemen Kristalloflex-X Ray generator using a cobalt anticathode driven by a personal computer through the Daco-PM interface was used.

Transmission Electron Microscopy and Electron Diffraction. A Jeol electron microscope (Jeol 100CX.2) was used.

Energy Dispersive Spectrometry. The spectra were obtained using a transmission electron microscope Jeol 100CXII equipped with a ASID 4D in the STEM mode and a Link AN 10,000. This equipment can detect neither boron nor oxygen. The relative amounts of iron and copper atoms were determined with a rather large probe size (35 nm).

Electron Energy Loss Spectrometry (EELS). The EELS data were recorded using a scanning transmission electron microscope (STEM) (VG HB 501 equipped with a Gatan 666 parallel EELS spectrometer), for the same sample as previously used for the normal TEM work.

Electron energy loss spectroscopy measures the energy loss suffered by high-energy incident electrons transmitted across the specimen and can be used to identify and measure the concentration of different atoms revealed by their characteristic core-ionization edges. Furthermore, we benefited from the spectrum-line acquisition mode installed on this machine,²³ which has been shown to provide a well-defined relationship between topography and chemistry at the nanometer scale.

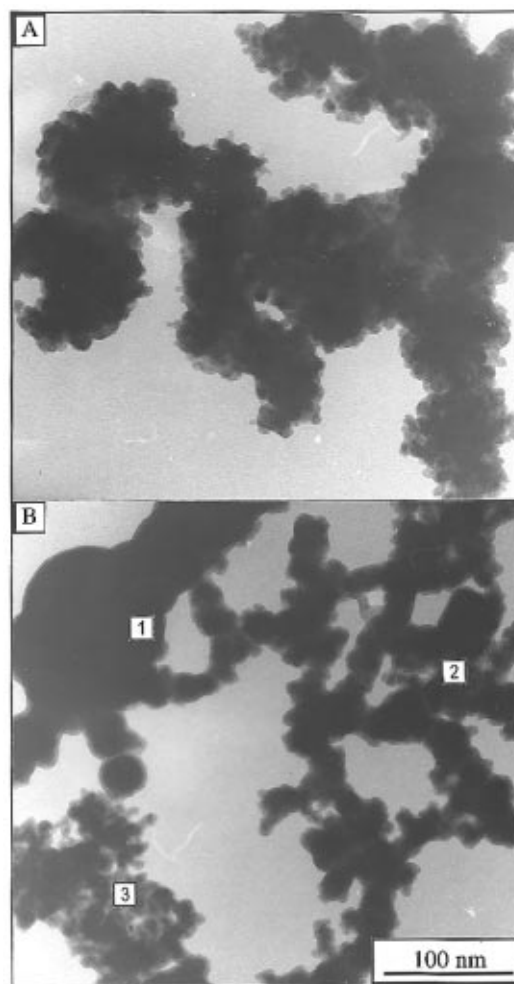


Figure 1. (A) Transmission electron microscopy image obtained for $x = 0.3$. EDS relative iron and copper concentrations are 32%Fe–68%Cu (B) Transmission electron microscopy image obtained for $x = 0.7$. EDS relative iron and copper concentrations are (1) 97%Fe–3%Cu; (2) 78%Fe–22%Cu; (3) 51%Fe–49%Cu.

3. Results

The experiments described below have been performed several times. One of the obvious reasons is the high oxidability of these alloys and composites. Furthermore, the large number of the experiments needed the fabrication of several samples. We first started to explore the behavior of the material at various x values, and we chose to perform a quantitative study at $x = 0.3$ and $x = 0.7$. These two values correspond to the regions in which alloys and composites are respectively formed. The choice of these values is also coherent to the data published in the literature from which alloys and composites are formed.

In both cases, microscopic and macroscopic studies have been performed, and we have performed quantitative studies in the two compositions which strongly differ. Several EELS spectra have been performed on various samples, and the data observed were similar.

3.1. Reduction of 30% Iron and 70% Copper Derivatives ($x = 0.3$): Alloy Formation.

The concentrations in $\text{Fe}(\text{AOT})_2$, $\text{Cu}(\text{AOT})_2$, and NaBH_4 are 3×10^{-2} , 7×10^{-2} , and 4×10^{-1} M, respectively. The synthesis leads to formation of homogeneous aggregates made of nanosized particles (Figure 1A). The particle size distribution is rather large, and the average diameter is in the range 5–15 nm. The EDS measurements show that aggregates contain 32% iron and 68% copper atoms. These values are close to the initial

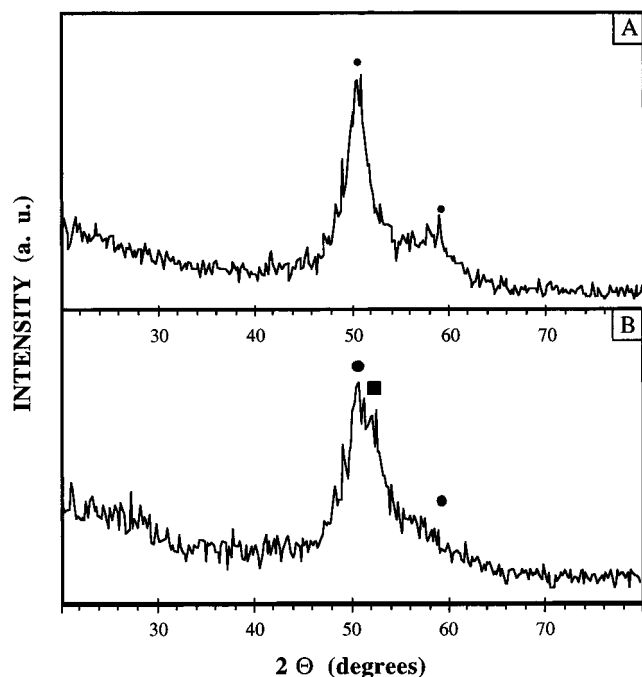


Figure 2. (A) X-ray diffraction patterns of $x = 0.3$ with a cobalt anticathode: $\lambda_{K\alpha} = 0.1789$ nm. (●) fcc Cu phase. (B) X-ray diffraction patterns of $x = 0.7$ with a cobalt anticathode: $\lambda_{K\alpha} = 0.1789$ nm. (●) fcc Cu phase; (■) bcc α -Fe phase.

composition, which indicates that all the metallic ions react to form the material. An fcc structure corresponding to metal copper particles obtained from X-ray diffraction (XRD) patterns is shown in Figure 2A. Neither oxide phase nor bcc structure due to an α -Fe phase is detected. This is confirmed by electron diffraction.

Local EELS analyses have been made of several 60×40 nm areas identified in Figure 3A. The relevant characterization edges are the B K edge at 188 eV, Fe $L_{2,3}$ edge at 708 eV, and Cu $L_{2,3}$ edge at 931 eV. A strong C K edge can be also seen at 284 eV. This is an amorphous type which is due to contamination under the electron beam by residual surfactant on the outer surface of the metallic nanoparticles. To detect all the useful signals of different weights and shapes, it has been useful to acquire them in the first difference mode (see Figure 3B).

To obtain quantitative values, the situation is rather complex, and it is necessary to follow different routes to measure the Cu/Fe ratios on one side and the B/Fe ratios on the other. In the first case, we use a normal background extrapolation technique for the signal displayed in the normal mode: Figure 4A (normalized iron signals) and 4B (corresponding copper signal from the intensity from which we derive the Cu/Fe relative concentrations using the relevant cross sections). In the second case, we use a least squares fitting of the second-derivative signal: Figure 4C (for normalized iron signal) and 4D (for the corresponding B edges). Table 1 shows that the Cu/Fe ratio ranges from 1.7 to 2.9, one area (no. 2) having a lower value (0.9). This is in agreement with the initial ratio of 2.33 of Cu(AOT)₂ and Fe(AOT)₂ used for the synthesis. As for the boron weight, it is not possible to evaluate it quantitatively, but only to monitor its variation with respect to the iron content. The comparison between parts B and D of Figure 4 suggests that the areas with the highest Cu/Fe ratios also have also the highest B/Fe values. This seems to be in contradiction with the hypothesis that the boron may stabilize the metastable structure of Fe–Cu alloys¹⁵ and should be checked in future systematic measurements.

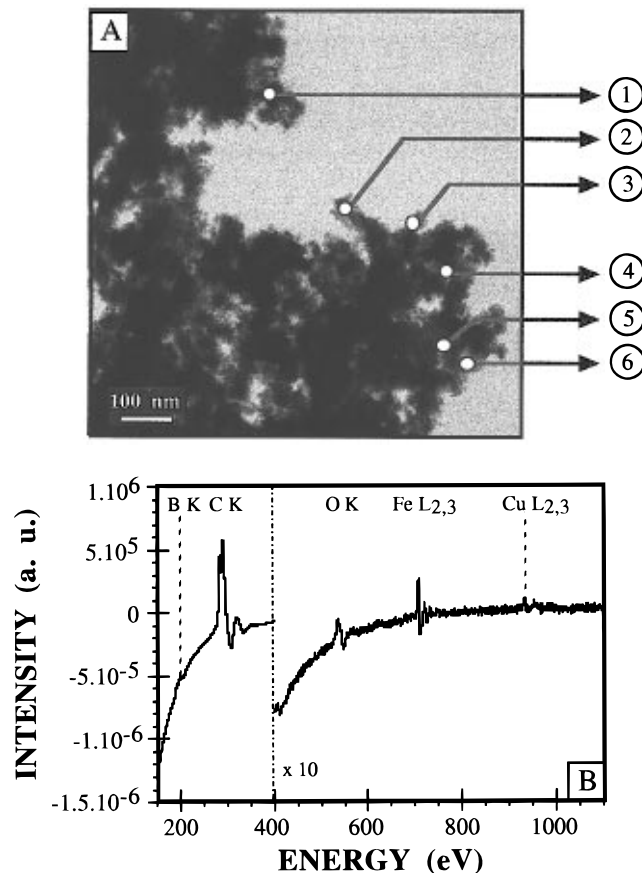


Figure 3. (A) STEM image of $x = 0.3$ sample for which EELS spectra are acquired in six different areas. The six spectra acquired in the first difference mode are represented in different ways. (B) EELS spectra acquired in the first difference mode corresponding to area no. 1.

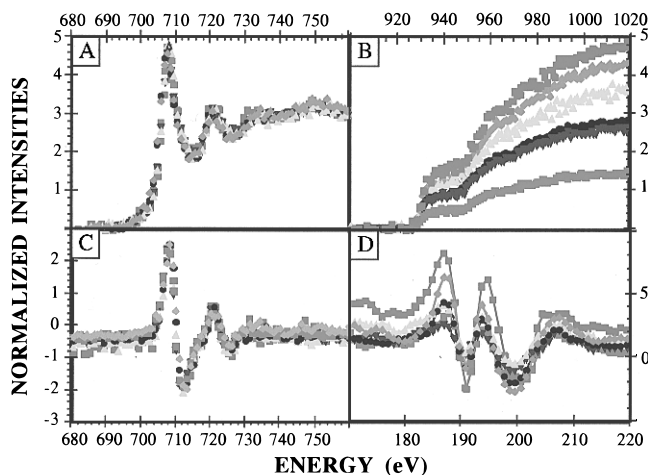


Figure 4. (A) EELS spectra displayed in normal mode and normalized on the Fe $L_{2,3}$ edge. (B) Corresponding Cu $L_{2,3}$ edges displayed in the normal mode, showing different Cu/Fe ratios. (C) EELS spectra displayed in the second difference mode on the Fe $L_{2,3}$ edge. (D) B K edge displayed in the second difference mode, showing different B/Fe ratios. (1) ■; (2) ■; (3) ▼; (4) ●; (5) ▲; (6) ◆.

TABLE 1: Cu/Fe Concentration Ratios on Various Areas of the $x = 0.3$ Sample

	area						
	1	2	3	4	5	6	nominal
Cu/Fe	2.86	0.93	1.67	1.89	2.33	2.50	2.33

To check the homogeneity in composition of the material at a nanoscale level, we acquire a sequence of spectra along the A'–B' line in the line-spectrum mode (Figure 5A). In the line-

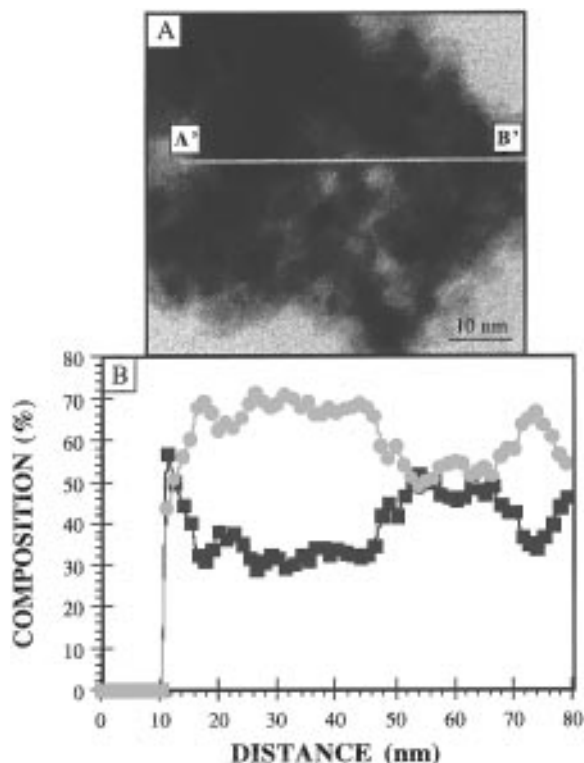


Figure 5. (A) STEM image of the $x = 0.3$ aggregate analyzed by EELS. (B) EELS chemical profiles of the $x = 0.3$ sample displaying a heterogeneous composition of iron and copper. Oxygen is not detectable. (●) copper; (■) iron.

spectrum mode, the 1 nm diameter electron probe is scanned automatically across the sample, and for each position of the probe an EELS spectrum is acquired. There are typically 64 or 128 spectra in the series, the probe step being determined by the magnification. In the present case, the probe step is 1.25 nm between each spectrum. The series of spectra can be processed a posteriori.²⁴ With the conventional quantification process used for a single spectrum and described above, an Cu/Fe concentration can be obtained (Figure 5B). It shows the simultaneous presence of iron and copper over the whole analysis region, with concentrations ranging from 30 to 55% for Fe and from 70 to 45% for copper.

The ^{57}Fe Mössbauer spectra are recorded at 4.2, 77, 300, and 330 K. The spectra recorded at 4.2 and 300 K are shown in Figure 6.

At 4.2 K, the spectrum can be fitted with two six-line magnetic hyperfine patterns. The majority component (85%) shows a distribution of hyperfine fields, represented by a histogram on the right of Figure 6 with a mean hyperfine field of 250 kOe and a width of 140 kOe. The minority component (15%) shows a hyperfine field of 455 kOe, typical of Fe^{3+} oxide.

At room temperature, three components can be resolved:

(i) A broad six-line pattern (75%) is represented by a histogram of hyperfine fields (right of Figure 6) with a mean field value of 200 kOe and width of 100 kOe.

(ii) A quadrupolar two-line pattern with $\delta = 0.4$ mm/s and $\Delta = 0.9(1)$ mm/s corresponds to Fe^{3+} (15%). This component is very probably the same as that observed at 4.2 K with a hyperfine field of 455 kOe, but in the superparamagnetic regime, where the hyperfine field fluctuates rapidly. This Fe^{3+} component could be due to small oxide particles or to an oxide layer surrounding the particles,¹⁸ not detected in XRD.

(iii) A quadrupolar doublet with $\delta = 1.1$ mm/s and $\Delta = 2.4$ mm/s probably corresponds to residual Fe^{2+} (10%). At 4.2 K, the Fe^{2+} component cannot be resolved.

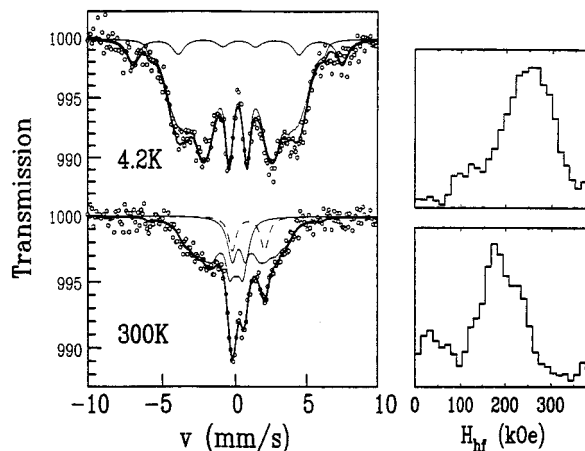


Figure 6. ^{57}Fe Mössbauer spectra for the $x = 0.3$ sample at $T = 300$ and 4.2 K. At 300 K, the minority doublet corresponds to residual Fe^{2+} , the other doublet to Fe^{3+} , and the broad sextet to metallic Fe–Cu or Fe–Cu–B alloy. At 4.2 K, the minority sextet corresponds to Fe^{3+} , and the majority sextet to the metallic alloy. The hyperfine field histograms of the metallic Fe are displayed at the right of the corresponding spectra.

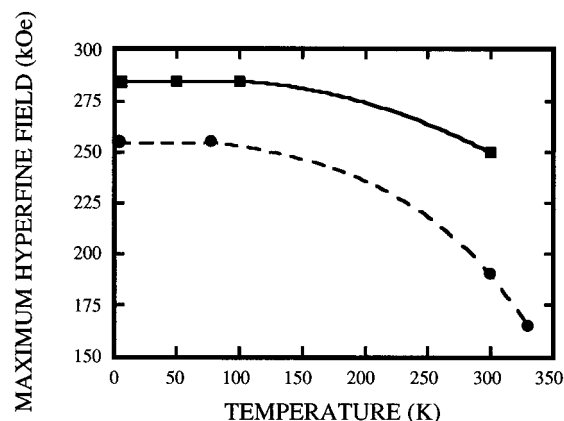


Figure 7. Mean hyperfine field, $H_{\text{hf}}^{\text{max}}$, of the alloy phase in the $x = 0.3$ (●) and $x = 0.7$ (■) samples as a function of temperature. The lines are visual guides. The low iron concentrated sample ($x = 0.3$) has a lower $H_{\text{hf}}^{\text{max}}$ than the $x = 0.7$ one.

The temperature variation of the mean hyperfine field, which corresponds to a metallic alloy, is plotted in Figure 7 as circles.

At room temperature, the magnetization curve shows no saturation for an 18 kOe magnetic field (Figure 8A). The saturation magnetization is deduced from zero extrapolation of M versus $1/H$. It is found to be ~ 1.1 emu/g. The low value of the saturation magnetization could be attributed either to atomic disorder inducing a negligible structural anisotropy or to a decrease in Curie temperature when alloys are formed.^{7,8,11,25–27} The low value of the coercivity field (24 Oe) is in good agreement with that obtained for alloys made by chemical reduction of Fe^{2+} and Cu^{2+} in aqueous solution.¹⁵

3.2. Reduction of Iron and Copper Derivatives ($x = 0.7$).

Composite Formation. Except for the relative concentrations of $\text{Fe}(\text{AOT})_2$ and $\text{Cu}(\text{AOT})_2$, the synthesis was performed under the same experimental conditions as described above. The $\text{Fe}(\text{AOT})_2$ and $\text{Cu}(\text{AOT})_2$ concentrations were 7×10^{-2} M and 3×10^{-2} M, respectively. A transmission electron microscopy (TEM) pattern (Figure 1B) shows particles differing by their sizes and shapes (large chains and spherical particles). The X-ray diffraction pattern (Figure 2B) exhibits the fcc and bcc phase. The fcc phase is due to copper metal phase whereas the bcc phase corresponds to an α -Fe phase. No oxide phase is detected. From the energy dispersive spectrometry (EDS)

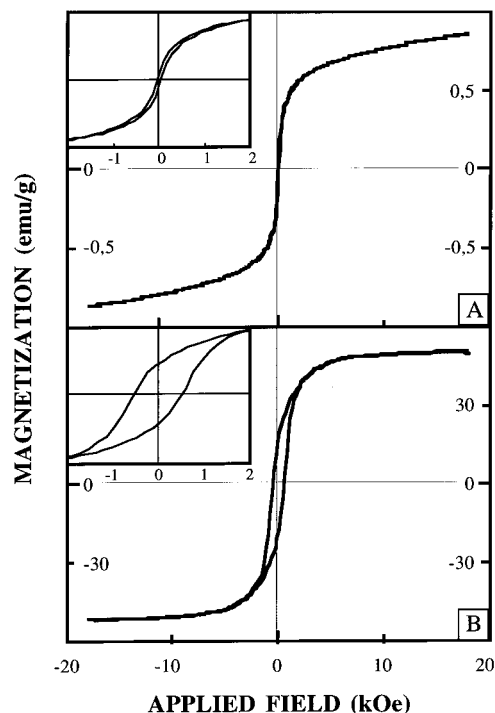


Figure 8. Room temperature magnetization plots of (A) $x = 0.3$ powder and (B) $x = 0.7$ powder. The insets are a magnification of the main curve.

analysis, the Cu/Fe ratio varies markedly with the size and shape of the aggregates. The broadest chains contain the largest number of Fe atoms, whereas in smaller aggregates, equal quantities of Fe and Cu are detected. This heterogeneity in composition is confirmed by EELS measurements. A line spectrum is recorded across variously shaped and sized nanophases (Figure 9A). Figure 9B shows the chemical profiles obtained from this spectrum line.

Different zones exist.

(i) On the left side of the image ($A'-B'$), the nanoparticles' average diameter is in the 15–40 nm range. Figure 9B shows that the average of copper, boron, and oxygen is 65, 20, and 15%, respectively. No iron is detectable. No oxide is detected by XRD, whereas oxygen is observed by EELS. This is probably due to passivation of particles during air exposure before EELS experiments, which concerns only the outer areas of the specimen where oxide is more likely to be present. Boron and oxygen concentrations are correlated. This can be attributed to formation of borate (B_2O_3) at the particle surfaces. The concentration of iron in the $A'-B'$ zone is less than 0.3%.

(ii) On the right side of the image shown in Figure 9A, zone $C'-D'$, a large chain (120–220 nm diameter) is observed. Less than 1.5% of copper is present. The major part of the material consists of iron (~80%), boron (<10%), and oxygen (~10%). The chain is also superficially oxidized.

(iii) In the central region ($B'-C'$), the size of the particles is intermediate. The four elements (Fe, Cu, B, O) are present. The percentage of these varies along the $A'-D'$ line. Here, the "alloying" effect, i.e., an intermediate composition of Fe and Cu, may in fact be mostly due to a projection averaging of particles of different composition.

Figure 10 shows a perspective view of the sequence of spectra acquired across the $A'-D'$ line (Figure 9), with the Fe $L_{2,3}$ edge and the Cu $L_{2,3}$ edge.

The ^{57}Fe Mössbauer spectra are recorded at 4.2, 50, 100, and 300 K (Figure 11). At all temperatures, the spectra are fitted with two components:

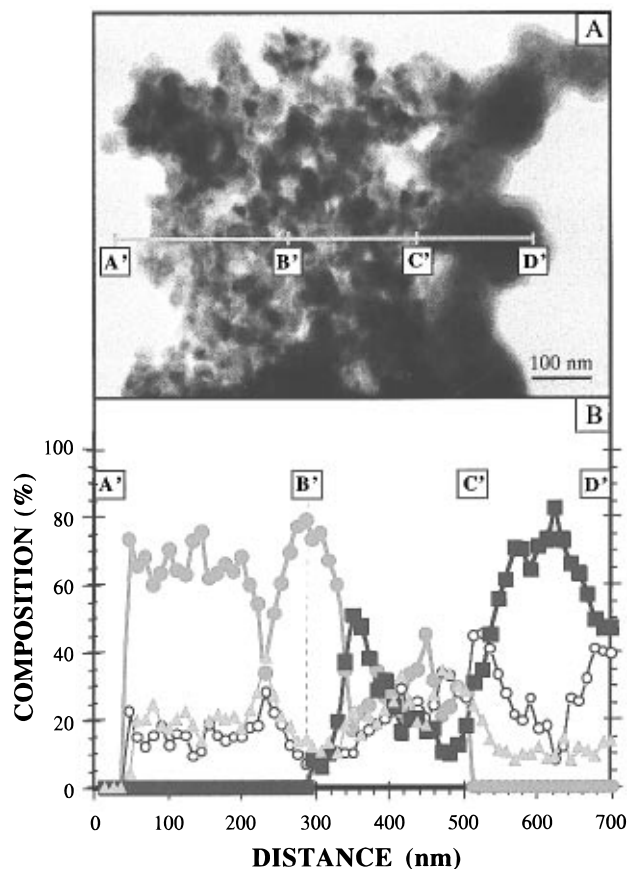


Figure 9. (A) TEM image of the aggregate with different morphologies analyzed by EELS along the $A'-D'$ axis. (B) EELS chemical profiles of composite material displaying two local iron/copper ratios depending on the morphology. On the left side of the image ($A'-B'$) are aggregated nanoparticles of pure copper with low oxide content. On the right ($C'-D'$), a pure iron chain is observed. ●: copper; ■: iron; ▲: boron; ○: oxygen.

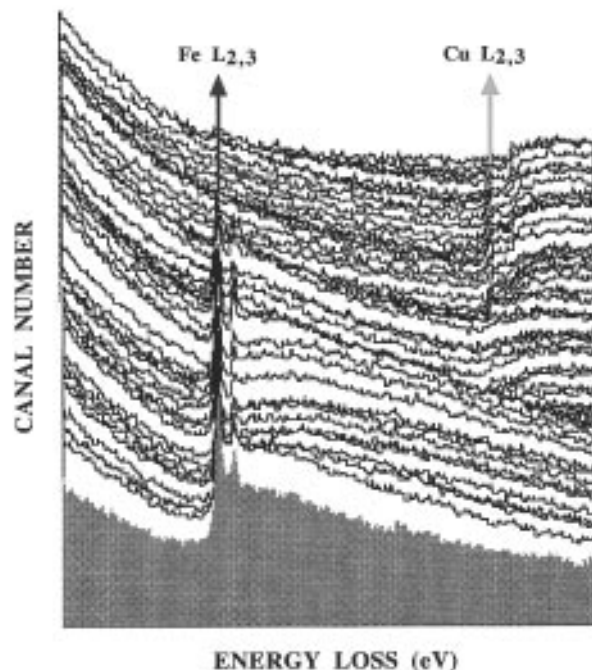


Figure 10. Three-dimensional representation of a spectrum line acquired across a set of aggregated particles displayed in Figure 9.

(i) A major component (75%) shows a broad distribution of hyperfine fields, which is represented with a histogram (right of Figure 11). The peak at 340 kOe in the histogram is

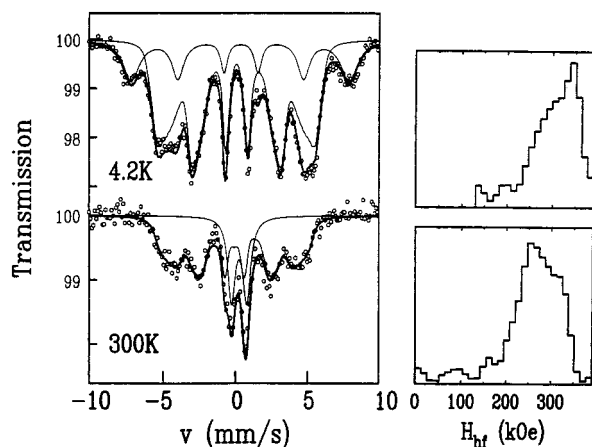


Figure 11. ^{57}Fe Mössbauer spectra for the $x = 0.7$ sample at $T = 300\text{ K}$ and 4.2 K . At 300 K , the doublet corresponds to the Fe^{3+} superparamagnetic oxide above its blocking temperature, and the sextet corresponds to metallic iron (amorphous alloy and $\alpha\text{-Fe}$). At 4.2 K , the component with the largest hyperfine field value corresponds to the Fe^{3+} oxide below its blocking temperature; the other sextet corresponds to metallic Fe ($\alpha\text{-Fe}$ and alloy). The hyperfine field histograms of the metallic Fe are displayed at the right of the corresponding spectra.

attributed to an $\alpha\text{-Fe}$ phase. In this distribution, the mean hyperfine field varies from a value $\sim 300\text{ kOe}$ at 4.2 K to $\sim 250\text{ kOe}$ at 300 K , with a root mean square deviation of about 60 kOe . These hyperfine field values indicate formation of alloys.

(ii) The minor component (25% relative intensity) shows a hyperfine field of 465 kOe at 4.2 K and a quadrupolar doublet between 50 and 300 K . Its isomer shift at 300 K is 0.5 mm/s . This corresponds to Fe^{3+} in an oxide phase²⁸ and shows superparamagnetic behavior with a blocking temperature $T_B \approx 50\text{ K}$. As in the previous sample, this Fe^{3+} component could be attributed to an oxide layer surrounding the particles,¹⁸ as detected by EELS experiments in the C'–D' zone.

Figure 7 shows the temperature variation of the mean hyperfine field of the major component (black squares). Over the whole temperature range, it is larger than that observed for $x = 0.3$.

The magnetization curve (Figure 8B) is characterized by a relatively large saturation, coercivity, and remanence with 51 emu/g , 531 Oe , and 18 emu/g , respectively.

4. Discussion

From the results presented above, the type of material obtained from colloidal assemblies differs with the initial iron to copper ratio in the synthesis.

At $x = 0.3$, formation of Fe–Cu alloys is demonstrated by the following:

- (i) A fcc structure corresponding to copper metal is obtained. No other structures are detected.
- (ii) By EDS, the average relative Cu/Fe ratio is 2.2, whereas by assuming a total reduction of $\text{Fe}(\text{AOT})_2$ and $\text{Cu}(\text{AOT})_2$, it is 2.33.
- (iii) From EELS experiments, the simultaneous presence of iron and copper on a nanoscale level over the length of analysis is observed.
- (iv) The six-line component of the Mössbauer spectra is large and attributed to an alloy formation.
- (v) As expected for an alloy formation, the temperature variation of the mean hyperfine field is smaller than that observed in the presence of $\alpha\text{-Fe}$ at $x = 0.7$ (Figure 7).

(vi) The magnetization decreases compared to other materials containing iron atoms. The small coercivity indicates alloy formation.

Hence, copper atoms are substituted by iron in the fcc matrix. However, from local structure measurements by EELS, the number of copper per iron atom is not constant (Table 1). It varies from 1.7 to 2.9 except in one local analysis, where it is 0.9. For a $\text{Fe}_{0.3}\text{Cu}_{0.7}$ alloy, if all the $\text{Fe}(\text{AOT})_2$ and $\text{Cu}(\text{AOT})_2$ react, the copper per iron ratio would be 2.33. From these data we can conclude that iron replaces copper atoms in its matrix but Cu/Fe per lattice differs slightly locally. This disorder of iron atoms in a fcc copper structure is supported by the broad Mössbauer spectra shown in Figure 6. The presence of boron in the material can be attributed to insertion in the alloy lattice. However, the presence of B_2O_3 on the outer surfaces cannot be excluded.

At $x = 0.7$, the formation of nanomaterials differing by their sizes, morphologies, and compositions is obtained. From the various measurements made, a clear correlation is observed between morphology and composition:

(i) Large chains containing mostly $\alpha\text{-Fe}$ aggregates are formed, as demonstrated by EDS (Figure 1B) and EELS (Figure 9). The latter technique confirms the coverage by an oxide layer. This is also in agreement with the XRD patterns (Figure 2B) and the Mössbauer spectra (Figure 11) exhibiting a component assigned to $\alpha\text{-Fe}$.

(ii) Copper nanoparticles with less than 1 or 2% iron content are formed, which are also covered with borate derivatives as demonstrated by the good correlation between the O and the B signals over this specimen area in the EELS measurement.

(iii) Compounds showing variable contents of both Fe and Cu (see intermediate zone B'–C' in Figure 9B) are formed, with a morphology made of a compact aggregation of small clusters. Two types of interpretation are then to be put forward: (i) an averaging of the concentrations along the beam direction, corresponding to nanoparticles made mainly of iron and copper, in which case the specimen would be a true "nanocomposite" of iron and copper particles; (ii) a real alloying effect within these small particles. Support for this interpretation is provided by Figure 10, which emphasizes the change in the fine structure observed at both Cu and Fe edges. The steep profile at the Cu $L_{2,3}$ edge (which is likely due to oxidation and empty d states) clearly disappears immediately and changes into a rounded profile as soon as iron and copper coexist along a beam trajectory. This reveals a reduced sensitivity of copper to oxidation in this zone, which could correspond either to an alloying effect or to a reduction of free surfaces due to a higher compactness of the nanoparticle aggregates. On the other hand, the Mössbauer spectra demonstrate the existence of an iron-based component, due to either Fe–B, Fe–Cu, or Fe–Cu–B.

All together this diversity of morphologies, chemistry, and magnetic properties shows that the products obtained with this iron-rich concentration ($x = 0.7$) are markedly different from the "alloying" behavior established in the copper-rich case ($x = 0.3$), and can be attributed to "composite-type" nanomaterials.

5. Conclusion

In this paper, we have shown that the use of functionalized surfactant favors the formation of Fe–Cu–B nanosized alloys and composites. To obtain an alloy, the amount of Fe^{2+} present in the chemical reaction must be limited. Fe–Cu–B alloys are obtained for chemical reduction of 30% $\text{Fe}(\text{AOT})_2$ and 70% $\text{Cu}(\text{AOT})_2$ ($x = 0.3$). For a higher iron concentration ($x = 0.7$), the amount of iron included in the copper fcc structure strongly changes and heterogeneous materials are obtained. In particular,

formation of an α -Fe phase occurs, whereas this is not the case when the initial percentage of Fe^{2+} is equal or inferior to 0.3. Hence by varying the relative percentage of iron versus copper, composite and alloyed Fe—Cu—B materials are formed.

References and Notes

- (1) Tracy, M. J.; Groza, J. R. *Nanostruct. Mater.* **1992**, *1*, 369.
- (2) Siegel, R. *Nanostruct. Mater.* **1993**, *3*, 1.
- (3) Higashi, K.; Mukai, T.; Tanimura, S.; Inoue, A.; Masumoto, T.; Kita, K.; 4htera, K.; Nagahora, J. *Scr. Metall.* **1992**, *26*, 191.
- (4) Linderroth, S.; Morup, S. *J. Appl. Phys.* **1991**, *69* (8), 5256.
- (5) Molnar, A.; Smith, G. V.; Bartok, M. *Adv. Catal.* **1989**, *36*, 329.
- (6) Leslie-Pelecky, D. L.; Rieke, R. D. *Chem. Mater.* **1996**, *8*, 1770.
- (7) Sumiyama, K.; Nakamura, Y. *J. Magn. Magn. Mater.* **1983**, *35*, 219.
- (8) Chien, C. L.; Liou, S. H.; Kofalt, D.; Yu, W.; Egami, T.; McGuire, T. R. *Phys. Rev. B* **1986**, *33* (5), 3247.
- (9) Uenishi, K.; Kobayashi, K. F.; Nasu, S.; Hatano, H.; Ishihara, K. N.; Shingu, P. H. *Z. Metallkd.* **1992**, *83* (2), 132.
- (10) Yavari, A.; Desre, P. J.; Benameur, T. *Phys. Rev. Lett.* **1992**, *8*, 2235.
- (11) Jiang, J. Z.; Gonser, U.; Gente, C.; Bormann, R. *Appl. Phys. Lett.* **1993**, *63* (8), 1056.
- (12) Jiang, J. Z.; Gonser, U.; Gente, C.; Bormann, R. *Appl. Phys. Lett.* **1993**, *63* (20), 2768.
- (13) Jiang, J. Z.; Chen, F. T. *J. Phys.: Condens. Matter* **1994**, *6*, L343.
- (14) J. Z.; Jiang, Q. A.; Pankhurst, C. E.; Johnson, C.; Gentes; Bormann, R. *J. Phys. Condens. Matter* **1994**, *6*, L227.
- (15) Chow, G. M.; Ambrose, T.; Xiao, J. Q.; Twigg, M. E.; Baral, S.; Ervin, A. M.; Qadri, S. B.; Feng, C. R. *Nanostruct. Mater.* **1992**, *1*, 361.
- (16) Saida, J.; Inoue, A.; Masumoto, T. *Metall. Trans. A* **1993**, *22*, 2125.
- (17) Saida, J.; Inoue, A.; Masumoto, T. *Mater. Sci. Eng.* **1994**, *A179/A180*, 577.
- (18) Linderroth, S.; Morup, S.; Bentzon, M. D. *J. Mater. Sci.* **1995**, *30*, 3142.
- (19) Glavee, G. N.; Klabunde, K. L.; Sorensen, C. M.; Hadjipanayis, G. C. *Langmuir* **1994**, *310*, 4726.
- (20) Glavee, G. N.; Klabunde, K. L.; Sorensen, C. M.; Hadjipanayis, G. C. *Inorg. Chem.* **1995**, *34*, 28.
- (21) Eckert, J.; Holzer, J. C.; Krill, C. E.; Johnson, W. L. *J. Appl. Phys.* **1993**, *73* (6), 2794.
- (22) Petit, C.; Lixon, P.; Pileni, M. P. *Langmuir* **1991**, *7*, 2620.
- (23) Colliex, C.; Tencé, M.; Lefèvre, E.; Mory, C.; Gu, H.; Bouchet, D.; Jeanguillaume, C. *Mikrochim. Acta* **1994**, *114/115*, 71.
- (24) Tencé M.; Quartuccio, M.; Colliex, C. *Ultramicroscopy* **1995**, *58*, 42.
- (25) Shen, J.; Li, Z.; Yan, Q.; Chen, Y. *J. Phys. Chem.* **1993**, *97*, 8504.
- (26) Ma, M.; Atzmon, M.; Pinkerton, F. E. *J. Appl. Phys.* **1993**, *74*, 955.
- (27) Sumiyama, K.; Nishi, K.; Nakamura, Y.; Manns, V.; Scholz, B.; Privik, M.; Keune, W.; Stamm, W.; Dumpich, G.; Wassermann, E. F. *J. Magn. Magn. Mater.* **1991**, *96*, 329.
- (28) Janot, C. *L'Effet Mössbauer et ses applications*; Masson, Ed.; 1972.